A dynamic model of a Cardan joint to evaluate the effect of elasticity and manufacturing errors

Marco Cirelli*

Department of Mechanical Engineering,
University Niccolò Cusano,
Via Don Carlo Gnocchi, 3,
00166 Roma, RM, Italy
Email: marco.cirelli@uniroma2.it
*Corresponding author

Valerio Rossi, Pier Paolo Valentini and Ettore Pennestrì

Department of Enterprise Engineering,
University of Rome Tor Vergata,
Via del Politecnico, 1,
00133, Roma, Italy
Email: valerio.rossi@uniroma2.it
Email: valentini@ing.uniroma2.it
Email: pennestri@mec.uniroma2.it

Abstract: Cardan joint is a key component in many mechanical applications. Due to the redundancy of kinematic constraints, the accurate determination of reaction forces and the assessment of dynamic effects caused by joint tolerances are very challenging tasks. This paper presents a computer-aided multibody modelling approach for the simulation of a Cardan joint with manufacturing errors. During the modelling phase, the elasticity of flexible bodies is lumped and the joint compliance is taken into account using concentrated non-linear spring elements. Numerical examples have been developed and discussed in order to test the feasibility of the proposed methodology.

Keywords: cardan joint; universal joint; flexibility; tolerance; elasticity; elastic coupling.

Reference to this paper should be made as follows: Cirelli, M., Rossi, V., Valentini, P.P. and Pennestrì, E. (2021) 'A dynamic model of a Cardan joint to evaluate the effect of elasticity and manufacturing errors', *Int. J. Vehicle Performance*, Vol. 7, Nos. 1/2, pp.136–155.

Biographical notes: Marco Cirelli received his BS and MS from the University of Rome Tor Vergata in 2014 and 2016 respectively. In 2020 he received his PhD on Design, Manufacturing, and Operations in Engineering working on multibody dynamics of transmission systems. Currently, he is a Research Fellow and Lecturer at the University "Niccolò Cusano" in Rome where he teaches the course of Applied Mechanics. His research interests are multibody dynamics, compliant

mechanisms, vibration-dampers, structural analysis, optimisation methods, and 3D design methods. He took part in several research projects funded by national and international institutions and industries.

Valerio Rossi received his Master's degree in Mechanical Engineering at the University of Rome Tor Vergata in 2011. In 2015 he earned his PhD in Industrial Engineering at the University of Rome Tor Vergata. He collaborated with the European Spatial Agency. His research interests are aerospace, multibody dynamics, numerical methods, and friction problems.

Pier Paolo Valentini received his MS in Mechanical Engineering and PhD in Design of Mechanical Systems). He is an Associate Professor of Applied Mechanics at the University of Rome Tor Vergata and teaches the courses of Virtual Prototyping and Bioprosthesis. He chairs the Laboratory of Virtual Prototyping and Simulation and serves as an Associate Editor for *Mechanism and Machine Theory Journal*, published by Elsevier. His research interests are computational mechanics, virtual prototyping, dynamics, structural simulations, biomechanics, and innovative computer-aided methodologies. He authored more than 160 papers on referred Journals and 3 patents. He coordinated more than 60 research projects funded by national and international institutions and industries.

Ettore Pennestrì received Laurea in Mechanical Engineering (University of Rome, 1980), MS in Mechanical Engineering (Columbia University, 1987), Eng.Sci.D. (Columbia University, 1991). He is currently a Professor of Mechanics of Machines at University of Rome Tor Vergata. His main research interests are kinematics, mechanism design, powertrain analysis, machine dynamics, biomechanics. He authored more than 100 papers in referred journals. In 2018 and 2019 received an Associate Editor Award for from ASME Journal of Mechanical Design. He is a Member of the Honorary Editorial Board of Mechanism and Machine Theory.

1 Introduction

Cardan joint, or universal joint, is a widely used assembly in several mechanical applications that require to transmit a rotary movement between misaligned shafts. A Cardan joint main components are an input and output shafts with two forks and an intermediate cross link (Krishna et al., 2000; Seherr-Thoss et al., 2006; Sheu et al., 1996)), as shown in the general embodiment of Figure 1. Each fork has two circular holes that form revolute joints with the pins of the cross link.

In the ideal case, a Cardan joint is a spherical four-bar linkage where the revolute joints have intersecting axes, a geometric condition hard and expensive to match. Only two kinematic pairs are strictly required to connect the cross with the forks. In actual Cardan joints there are four kinematic pairs evenly distributed. This redundancy in kinematic constraints allows a distribution of reaction forces. To allow mobility also in presence of small manufacturing errors the revolute joints are substituted with cylindrical joints.

Figure 1 Cardan joint mechanical system: (a) assembled view and (b) exploded view (see online version for colours)

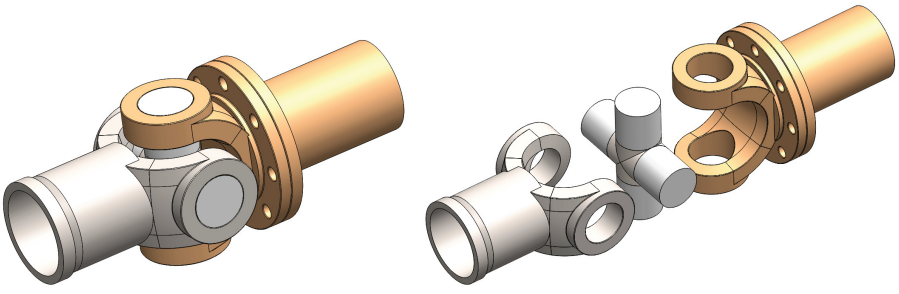

(a) (b)

The degrees-of-freedom of a spatial mechanical system can be evaluated by means of the Kutzbach formula

$$DOF = 6(\ell - j - 1) + \sum_{i=1}^{j} f_i \tag{1}$$

where DOF is the degree-of-freedom of the system, ℓ the number of bodies, j the number of joints and f_i the degree-of-freedom of the ith joint.

For the ideal Cardan joint there are $\ell = 4$ bodies, $j = 4$ joints (4 revolute joints RRRR), and $f_i = 1$. The straight application of the Kutzbach equation leads to $DOF = -2$ degrees-of-freedom. However, if one considers the Jacobian matrix rank deficiency due to the incidence of revolute joints axes at the centre of the cross, then the assembly has a single degree-of-freedom.

To explain the one-degree-of-freedom of Cardan joint, ideally a spherical RRRR linkage, is substituted with an RCCC linkage (one revolute and three cylindrical kinematic pairs).

The substitution has the following advantages:

- since the structure is statically determinate, all the generalised reaction forces components can be computed applying Newton-Euler equations only
- the mobility is guaranteed also in the presence of unavoidable misalignments of joint axes due to manufacturing errors.

In the ideal joint, the angular velocity of the output shaft depends on the angle α of misalignment between the shaft axes. Although the angular velocity of the driving shaft is constant, when $\alpha \neq 0°$ the output velocity experiences an oscillating behaviour. Therefore the transmission ratio τ is a function of the angle α, as expressed by the following relation

$$\tau = \frac{\cos\alpha}{1 - (\sin\alpha\cos\theta_{in})^2} \tag{2}$$

where θ_{in} is the rotation angle of the driving shaft.

Many papers regarding the kinematic analysis of Cardan joints are on the record (e.g., Daskalov (1990)). Freudenstein and his co-workers presented the first complete dynamic analysis of a Cardan joint (Fischer and Freudenstein, 1984; Chen and Freudenstein, 1986) developed within the framework of Clifford algebra.

When simulating the behaviour of a transmission chain with common multibody methodologies, Cardan joint is often included as a *black box*, by adding a simple kinematic coupling relationships between the relative velocities of the connected shafts.

The purpose of this investigation is to propose a more accurate modelling of the actual Cardan joint in order to evaluate reaction forces, the effects of manufacturing errors and elasticity in the transmission irregularities, as well as the forces transmitted to the frame. This last issue is important to assess vibration sources along the transmission driveline.

From a numerical simulation point of view, a complication is the redundancy of joint constraints in the actual Cardan. In this case, the evaluation of the reaction forces is not possible when the coupling between rigid bodies is modelled with kinematic constraint equations (Wojtyra, 2009).

Moreover, the effects of manufacturing and assembly errors, always present in the real mechanical parts, need to be simultaneously considered as well. In fact, the presence of these errors is somehow managed by the clearances and elasticity of the components which are in general neglected in a rigid body model with kinematic constraint equations.

Scientific literature often reports studies on universal joints by simplifying the mechanism topology. Suppression of the redundant constraints (e.g., Park et al. (1988)) is a widespread technique. Although the overall kinematic behaviour of the mechanical system in case of redundant constraints elimination is unchanged, the evaluation of the constraint reaction forces and torques is definitely prone to errors.

Other studies introduce clearances in revolute joints for overcoming the redundancies. As hinted by several authors (e.g., Cavacece et al. (2005)), a Cardan joint can be modelled as a RCCC spatial linkage. By making use of this technique, it is possible to evaluate the influence of manufacturing errors on the performances of the assembly (e.g., mechanical efficiency). On the other hand, the simulation of manufacturing and assembly errors is mandatory for an accurate design of transmission joint since their influence may be relevant to assess the safety of operating conditions (Cavacece et al., 2004; Hummel and Chassapis, 2000; Pezzuti et al., 2006; Valentini and Pezzuti, 2011). A more advanced formulation could foresee several errors at the same time following a certain statistic. Rameau et al. (2019) and Cecchini Emanuele (2004).

In order to account for the effects of elasticity and manufacturing errors and for a more accurate estimation of reaction forces under dynamic conditions, a new Cardan joint multibody model has been herein proposed. Errors due to the shape deformation of the fork's holes are not taken into account.

The methodology, that can be replicated within any CAE software tool with multibody simulation capabilities, is based on the replacement of kinematic constraints with dynamic constraints (penalty forces). This methodology, successfully applied in other studies (e.g., Koutsovasilis and Fruth (2012), Valentini (2014) and Askari et al. (2014)), has been herein extended to the Cardan joint and guidelines are given for tuning the damping and stiffness at the joints for a reliable simulation.

The paper is organised as follows. In Section 2, a description of the proposed approach is discussed. In Section 3, four test cases of a Cardan joint with different geometrical and dimensional errors are presented. The influence of the errors on the performance of the joint are evaluated in terms of kinematic parameters, such as the transmission ratio, and in terms of dynamic performances, such as reaction forces and moments. Section 4 reports the results of the numerical simulations and the comparisons between the proposed test cases. Section 5 depicts the final conclusion.

2 Model description

The proposed methodology removes the kinematic constraints of the moving revolute joints and replaces them with spring-damper elements. During simulation these generate restoring penalty forces proportional to the violation of the constraints.

The generalised reaction force components of revolute joints are exerted through the contact between the surfaces of the cross pins and that of the forks holes. This phenomenon can be somewhat reproduced by replacing the kinematic constraints with two springs at the extremity of the pin. The springs maintain the distance between the pin and hole surfaces within a given range. The tuning of spring stiffness is of paramount importance. High values may cause overshooting and peaks of the penalty forces thus generating a stiff behaviour of the system of differential equations.

Surface penetration must be also avoided. As deduced by Brutti et al. (2011), the position of the pin inside the hole generates different contact modes. In particular, as shown in Figure 3, four contact modes can be observed: no contact, one-point contact, two-points contact and uniform contact.

To account for this physical behaviour, as shown in Figure 2, in the model the kinematic constraints of each revolute joint connecting the cross link have been substituted with two non-linear springs at the extremities of the cross pin. Hence, the kinematic constraints of the cross revolute joints have been replaced with eight non-linear springs.

Figure 2 Non linear springs applied at the extremity of the cross joint (see online version for colours)

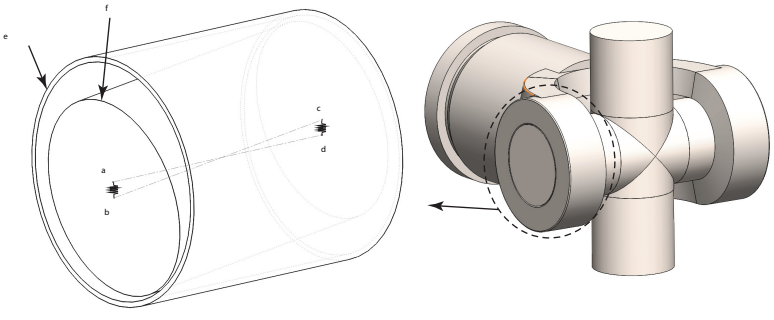

Figure 3 Joint contact types: (a) no contact; (b) one-point contact; (c) two-points contact and (d) uniform contact

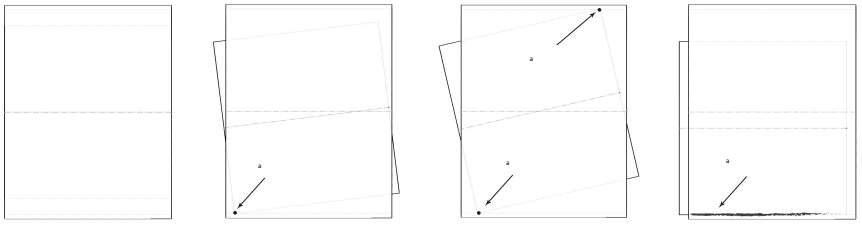

(a) (b) (c) (d)

The non-linear spring extremities are the centre of the fork hole O_1 and the centre of the pin of the cross O_2, as shown in Figure 4.

The force/displacement relationship of each non-linear spring, in case of uniform contact, can be defined using a formula by Young et al. (2011), based on the Hertz theory, and hereinafter reported for ready reference:

$$\delta_{O_1-O_2} = \frac{2F_c(1-\nu^2)}{\pi E}\left(\frac{2}{3} + \ln\frac{2D_H}{b} + \ln\frac{2D_P}{b}\right) \tag{3}$$

where:

- $\delta_{O_1-O_2}$ is the relative displacement between the centre of the hole O_1 and the centre of the pin O_2 in case of uniform contact
- F_c is the contact load per unit length
- D_H and D_P are the diameters of the hole and the pin respectively
- E and ν are the Young modulus and the Poisson coefficient respectively
- $b = 1.6\sqrt{F_c K_D C_E}$ is the width of the contact area
- $K_D = \dfrac{D_H D_P}{D_H - D_P}$ and $C_E = 2\dfrac{1-\nu^2}{E}$.

Table 1 reports the numeric parameters and elastic properties for the Cardan joint analysed in this work, where G is the shear modulus. The forks and the cross bodies are made of the same material therefore equal elastic characteristics are assumed for each joint component. The diameters of the hole and the pin are respectively $D_H = 76.2\,\mathrm{mm}$ and $D_P = 76\,\mathrm{mm}$. The length of the contact area is assumed $z = 22\,\mathrm{mm}$.

Figure 4 Non-linear spring between the centre of the hole O_1 and the centre of the pin O_2

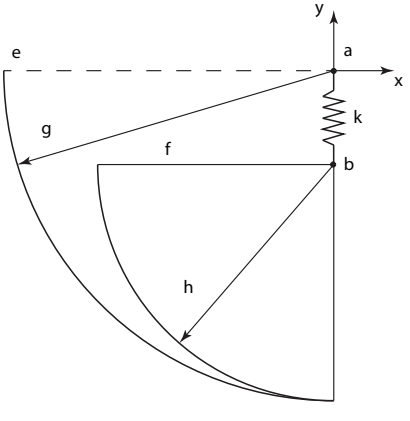

In case of one-point and two-points contact the relative displacement $\delta_{O_1-O_2}$ of equation (3) as reported in Brutti et al. (2011) becomes:

$$\delta'_{O_1-O_2} = H \cdot \delta_{O_1-O_2} \tag{4}$$

where H is a constant depending on pin and hole dimensions and clearance while $\delta'_{O_1-O_2}$ represents the new computed displacement.

The clearance between the pin and the hole is assumed to be 2% of the nominal diameter. From the charts reported in Brutti et al. (2011), the constant of equation (4) is $H = 6.9$.

Table 1 Elastic and dimensional properties of the Cardan joint

E	210 GPa
G	79 GPa
ν	0.28
K_D	38.1
C_E	$9 \cdot 10^{-12}\,\mathrm{GPa}^{-1}$

In order to simplify the force/displacement relationship and to handle a non recursive formula, a procedure of curve fitting, by means of quadratic functions, is herein adopted. Thus, with reference to Figure 5, the expression of the elastic force generated by the springs follows

$$F = k_1\delta^2 + k_2\delta + c\dot{\delta} \tag{5}$$

where F is the spring force, δ is the spring deformation, k_1 and k_2 are the coefficient of the parabolic approximating function and c is the damping coefficient. The stiffness values of each non-linear spring are computed using equations (3)–(5). The numeric values are reported in Table 2.

Figure 5 Force behaviour with respect to the spring deformation δ in case of uniform contact or one-point and two-points contact

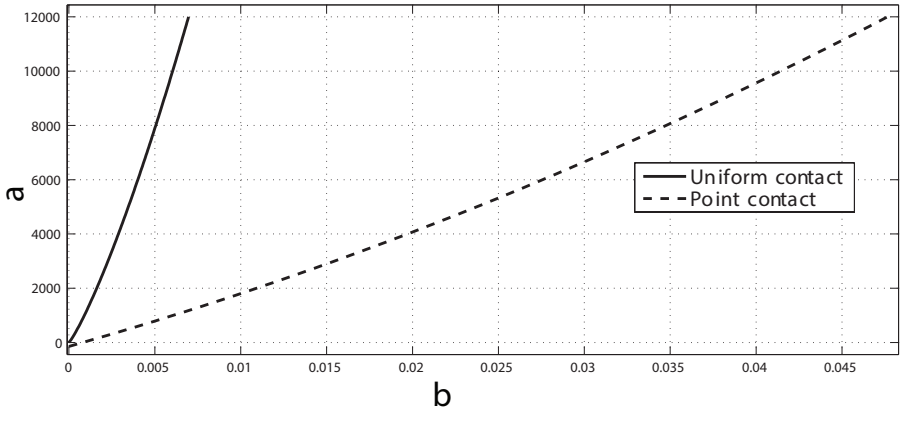

A damping term has been added to simulate the contact energy dissipation and to bound numerical instabilities. In order to estimate a feasible damping coefficient, each pin of the cross has been modelled as a cantilevered beam. In this case, the first circular frequency of the beam is

$$\omega = \frac{\pi^2}{l^2}\sqrt{\frac{EJ}{\rho A}} \tag{6}$$

where l is the length of the cross pin, J the area moment of inertia, ρ the density of the material and A the section area. The damping value can be estimated considering the critical damping of a cantilevered beam as follows

$$c = \xi 2m\omega \tag{7}$$

where ξ is the damping ratio and m the mass of the pin. A damping ratio of 5% is consistent for a Cardan joint made of alloy steel. Considering $J = 1.02 \cdot 10^{-7}\,\mathrm{m}^{-4}$, $\rho = 7.70 \cdot 10^{-6}\,\mathrm{kgm}^3$, $l = 36.41\,\mathrm{mm}$, $m = 0.32\,\mathrm{kg}$ and $A = 11.34 \cdot 10^{-4}\,\mathrm{m}^2$, the coefficient of damping assumed for each non-linear spring is $c = 3.71 \cdot 10^8\,\mathrm{Ns/m}$.

Table 2 Non-linear spring stiffness values

Stiffness	*Uniform contact*	*Point contact*
k_1	$7.5 \cdot 10^7\ \frac{\mathrm{N}}{\mathrm{mm}^2}$	$1.6 \cdot 10^6\ \frac{\mathrm{N}}{\mathrm{mm}^2}$
k_2	$1.2 \cdot 10^6\ \frac{\mathrm{N}}{\mathrm{mm}}$	$1.8 \cdot 10^5\ \frac{\mathrm{N}}{\mathrm{mm}}$

Figure 6 shows the eight spring penalty elements of the entire Cardan joint.

Figure 6 Non linear springs between each pin of the cross and the holes of the input and output fork (see online version for colours)

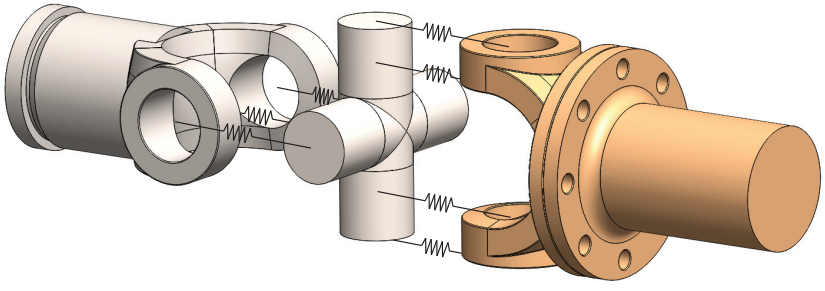

The dimensional errors may produce deformations of the entire joint structure in order to ensure the mobility. In this case, the elasticity of the structure and joint clearances play an important role and need to be included in the model to accurately simulate the dynamic system. In fact, the deformations can produce an hazardous level of stress in the structure. These effects must be taken into account also for a correct dimensioning and an assessment of mechanical fatigue phenomena.

In order to include the elasticity in the current multibody model, a discrete flexible model approach has been adopted. The bodies of the cross and the forks have been split in several sub-parts and then connected by bushings that simulate the elastic compliance of the structure. A bushing element is a six-component linear force acting between two bodies at a specific location. The mathematical expression of a bushing element is hereinafter reported

$$\vec{F} = -[K]\vec{x} - [C]\dot{\vec{x}} \tag{8}$$

where the stiffness matrix $[K]_{6\times6}$ and the damping matrix $[C]_{6\times6}$ are 6×6 diagonal matrices and $\vec{F}_{6\times1}$ is the vector containing both forces and torques.

In particular, the stiffness matrix is defined as follows

$$[K] = \begin{bmatrix} k_x & & & & & & \\ & k_y & & & & & \\ & & k_z & & & & \\ & & & k_{b_x} & & & \\ & & & & k_{b_y} & & \\ & & & & & k_{t_z} & \end{bmatrix} \tag{9}$$

where k_x, k_y and k_z are the stiffness terms referring to the linear displacement, k_{b_x} and k_{b_y} the bending stiffness terms along x and y direction and finally k_{t_z} is the torsional stiffness term along the z axis.

The cross body has been virtually split in five different bodies connected through four bushings $[K]_c$. Figure 7 reports the exploded view of the cross link where the cuts between the bodies are at the beginning of each pin of the cross.

Figure 7 Discrete flexible model of the Cardan joint cross: (a) exploded view and (b) reference frame (see online version for colours)

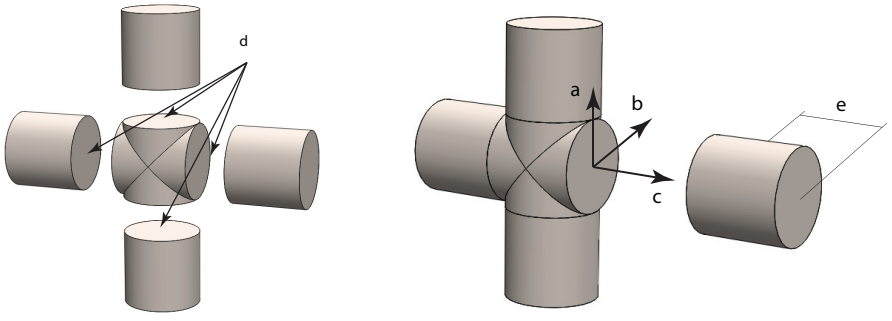

(a) (b)

Similarly, each fork has been split in three different parts linked by means of 2 bushings $[K]_f$. Figure 8 reports the fork sub-parts divided at the attachment of each fork extremity. The outer sub parts of each component are considered as a cantilever beams. For the cross body this approximation is rather justified by the simple geometry of the structure. For the forks, the complex shape of the outer sections has been simplified with a constant section cantilevered beam.

The linear stiffness values are estimated considering the shear and axial stiffness terms of the approximating beam by using the following equations

$$k_x = \frac{GA}{\chi_x} \quad , \quad k_y = \frac{GA}{\chi_y} \quad , \quad k_z = \frac{EA}{l} \tag{10}$$

where χ_x and χ_y are the shear factors.

The bending and torsional stiffness terms are computed as follows

$$k_{b_x} = \frac{EJ_x}{l} \quad , \quad k_{b_y} = \frac{EJ_y}{l} \quad , \quad k_{t_z} = \frac{GJ_p}{l} \tag{11}$$

where J_x and J_y are the area moment of inertia around x and y directions respectively while J_p is the polar moment of area.

Table 3 reports the bending stiffness values for the cross and the forks. The numerical parameters of the cross have already been introduced, except for the shear factor of a circular section $\chi_c = 1.11$. For the fork the following numerical values are adopted: $A = 12.18 \cdot 10^{-4}\,\mathrm{m}^2$, $J_x = 4.14 \cdot 10^{-8}\,\mathrm{m}^4$, $J_y = 3.42 \cdot 10^{-7}\,\mathrm{m}^4$, $J_p = 3.83 \cdot 10^{-7}\,\mathrm{m}^4$, $l = 37.49\,\mathrm{mm}$, $\chi_f = 1.2$.

Figure 8 Discrete flexible model of the Cardan joint fork: (a) exploded view and (b) reference frame (see online version for colours)

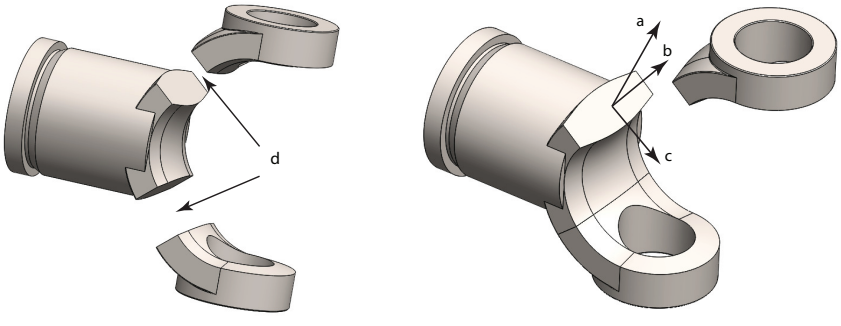

(a) (b)

Table 3 Stiffness values for the cross $[K]_c$ and fork $[K]_f$ bushings

Stiffness	*Cross bushings*	*Fork bushings*
k_x [N/m]	$2.21 \cdot 10^9$	$2.14 \cdot 10^9$
k_y [N/m]	$2.21 \cdot 10^9$	$2.14 \cdot 10^9$
k_z [N/m]	$6.54 \cdot 10^9$	$6.82 \cdot 10^9$
k_{b_x} [Nm]	$5.90 \cdot 10^5$	$2.32 \cdot 10^5$
k_{b_y} [Nm]	$5.90 \cdot 10^5$	$1.91 \cdot 10^6$
k_{t_z} [Nm]	$4.44 \cdot 10^5$	$8.08 \cdot 10^5$

The same stiffness values are assumed for the bushings on the input and output forks.

The mass of each part has been lumped at the extremities.

The damping ratio has been estimated to $\xi = 4\%$ of the critical damping value for the cantilevered beam approximation. The following formula is used for the torsional damping coefficient evaluation

$$c = \xi 2\sqrt{kJ} \tag{12}$$

Figure 9 reports the proposed flexible multibody model of a Cardan joint.

3 Numerical simulations

A flexible multibody model of a Cardan joint has been developed using the methodology described in the previous section.

Figure 9 Discrete flexible multibody model with bushings $[K]_f$ on each fork and $[K]_c$ on the cross (see online version for colours)

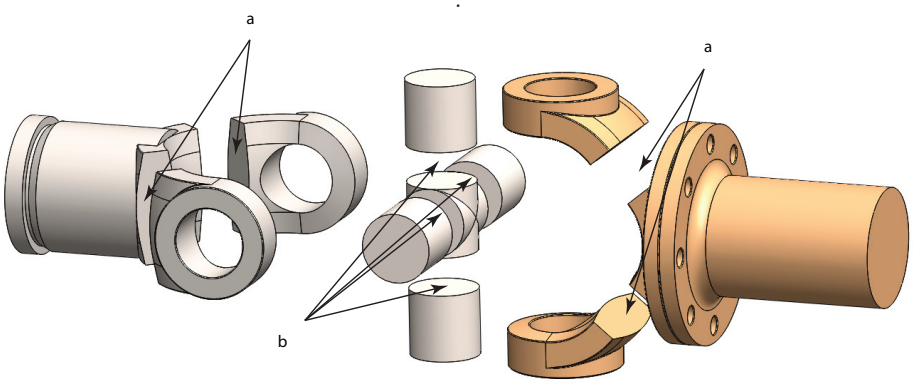

A Cardan joint with compliances, but without any manufacturing error, has been analysed in order to have a preliminary assessment of the model.

The comparison of the numerical simulation results between this model and the analytic solution, see Seherr-Thoss et al. (2006), has been carried out in order to test the accuracy and reliability of the discrete flexible model developed.

The results of the simulation, in terms of kinematic and dynamic parameters, show a transient effect during the first shaft revolutions which is something expected from a numerical point of view. In this phase each bushing and each spring is loaded. Steady state behaviour is observed after twenty driving shaft revolutions. After that transient phase the simulation results match those of the analytic solution.

Every analysis has been solved by using a `GSTIFF` integrator and 20 revolutions of the input shaft have been simulated in order to reach a stable and reliable values of all dynamic variables. The last revolution has been considered for the interpretation of the results.

Four types of errors have been introduced in the model and studied independently:

a localisation error on the axis of one cross pin (*Pos cross*)

b angular error on the axis of one cross pin (*Ang cross*)

c localisation error on the axis of one output fork extremity (*Pos fork*)

d angular error on the axis of one output fork extremity (*Ang fork*).

Figure 10 shows the cases investigated where the error amplitudes have been amplified for visual purpose. The identification numbers of the bushings for the cross and for the output fork are also highlighted.

The error amplitudes have been chosen consistently with the ISO 2768-f (precise manufacturing quality): $0.1\,\mathrm{mm}$ for linear error and 0.5° for angular error. Each simulation has been performed imposing a resisting torque of $T_r = 100\,\mathrm{Nm}$ on the driven shaft, a constant input velocity of $\omega = 500\,\mathrm{rpm}$ on the driving shaft and angles of misalignment of $\alpha = 0^\circ$ and $\alpha = 15^\circ$, as shown in Figure 11.

Figure 10 Error cases analysed: (a) localisation error on the cross pin 1; (b) angular error on the cross pin 1; (c) localisation error on the output fork extremity 1 (*Pos fork*); (d) angular error on the output fork extremity 1 (*Ang fork*) (see online version for colours)

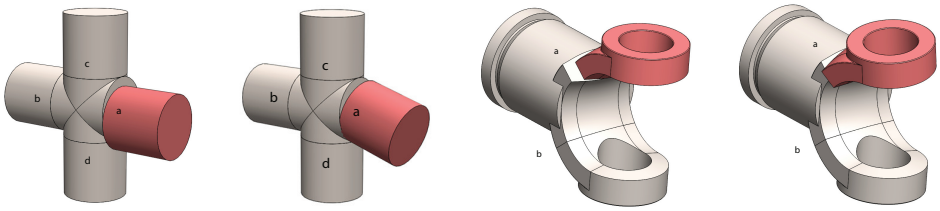

Figure 11 Kinematic and dynamic conditions for the numerical simulations (see online version for colours)

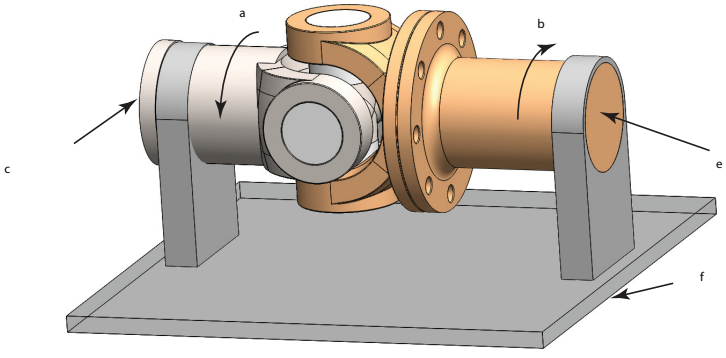

4 Results and discussion

The kinematic influence of the errors introduced for each test case has been investigated.

The velocity ratio relative error with respect to the analytic solution of the ideal case is adopted as kinematic performance parameter and is defined as follows

$$\Psi = \frac{\tau - \tau_{an}}{\tau} \tag{13}$$

where τ is the speed ratio of each numerical simulation and τ_{an} the speed ratio of the analytic solution defined by equation (2).

Figure 12 reports the speed ratio relative error of the joint with misalignment angles of $\alpha = 0°$ and $\alpha = 15°$. The labels visible in the plot legend symbolised the error cases mentioned in Section 3.

The speed ratio relative error presents mainly the same behaviour for each test case. If the misalignment angle α is increased, then the difference with respect to the analytic solution also grows. However, the influence on the transmission ratio of the investigated test cases appears marginal and the overall kinematics is preserved.

Figure 12 Gear ratio relative error $[\Psi]$: (a) misalignment angle $\alpha = 0°$ and (b) misalignment angle $\alpha = 15°$

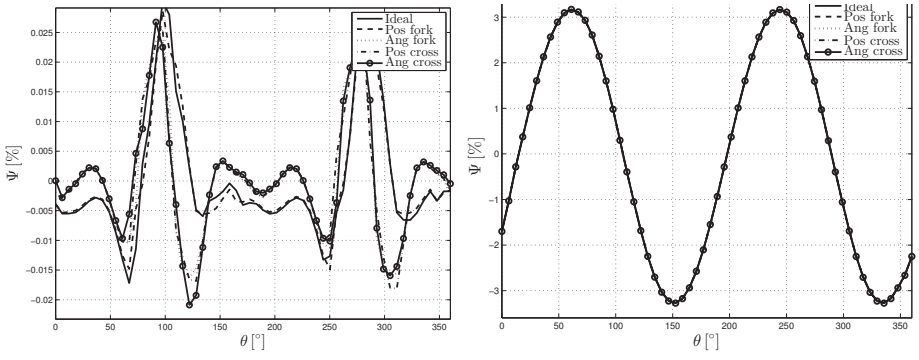

(a) (b)

Regarding the bushing force and torque, only the modulus of each vector is hereinafter discussed.

In order to compare the dynamic simulation results with respect to the ideal case, a relative error for each case has been computed as follows

$$\Gamma_F = \frac{F - F_{id}}{F_{id}} \cdot 100 \quad , \quad \Gamma_T = \frac{T - T_{id}}{T_{id}} \cdot 100 \tag{14}$$

where Γ_F and Γ_T are the relative bushing force and torque errors respectively, Γ_{id} and T_{id} the maximum bushing force and torque referring to the ideal model, F and T the maximum bushing force and torque for each error case.

Figures 13 and 14 report the forces and torques acting on the cross bushings 1 and 2 in case of a misalignment angle of $\alpha = 0°$.

Figure 13 Cross bushing force vs input shaft angle θ for misalignment angle of $\alpha = 0°$: (a) cross bushing 1 and (b) cross bushing 2

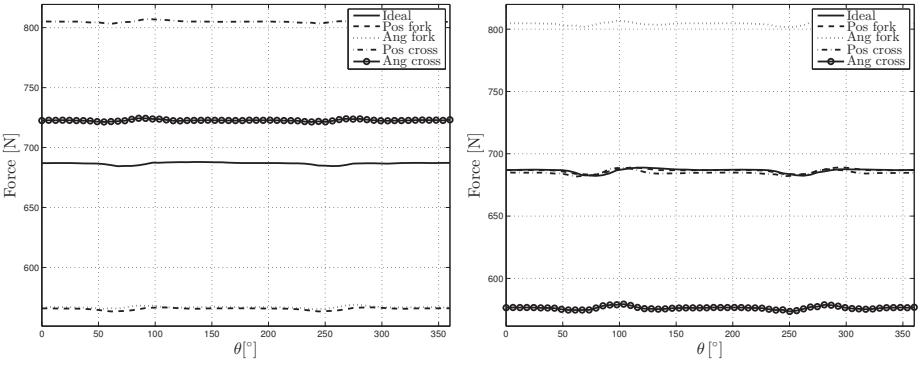

(a) (b)

Figures 15 and 16 show the force and torque plots of the cross bushings 1 and 2 in case of an angle of $\alpha = 15°$.

Figure 14 Cross bushing torque vs input shaft angle θ for misalignment angle of $\alpha = 0°$: (a) cross bushing 1 and (b) cross bushing 2

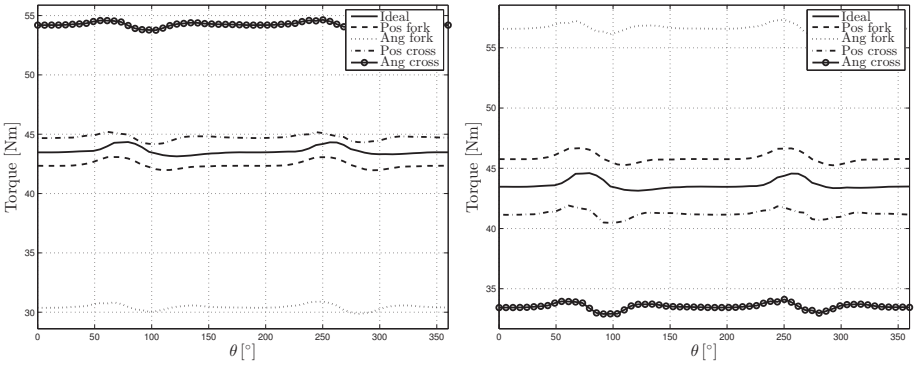

Figure 15 Cross bushing force vs input shaft angle θ for misalignment angle of $\alpha = 15°$: (a) cross bushing 1 and (b) cross bushing 2

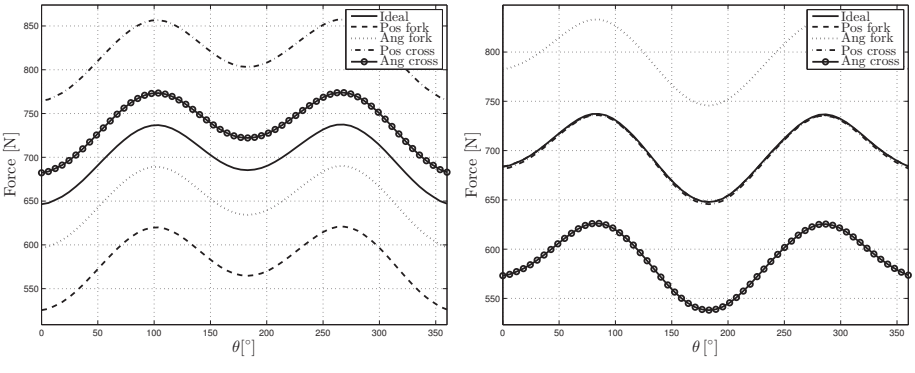

Both the localisation and the angular errors are applied on the cross bushing 2, as shown in Figure 10.

Tables 4 and 5 report the maximum values of the relative cross bushing force and torque plots, see equation (14), assuming a misalignment angle of $\alpha = 0°$ and $\alpha = 15°$.

It can be observed that the effects of the manufacturing errors on the cross bushings are located entirely on the bushings 1 and 2. The forces and torques acting on the cross bushings 3 and 4 are not herein reported.

A significant influence on the torque reactions is due to the angular errors *Ang cross* and *Ang fork*. Cross bushing 2 experiences also an increase of the force reaction greater than 15% in presence of angular errors. Since the localisation error is applied on cross bushing 1, the most relevant influence, in terms of force reaction, appears on this bushing. The dynamic reaction of the cross bushing 2 is apparently not affected by the error of localisation introduced for the *Pos fork* and *Pos cross* test cases.

The increase of misalignment angle α from $0°$ to $15°$ seems to mitigate the reactions on the cross bushings.

Figure 16 Cross bushing torque vs input shaft angle θ for misalignment angle of $\alpha = 15°$: (a) cross bushing 1 and (b) cross bushing 2

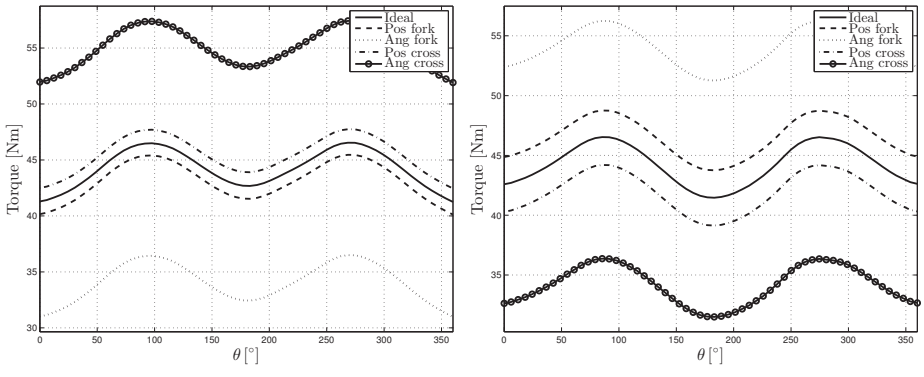

Table 4 Maximum relative cross bushing force and torque errors [%] for a misalignment angle of $\alpha = 0°$

Cross / *Test*	*Bushing 1*		*Bushing 2*		*Bushing 3*		*Bushing 4*	
	Γ_F	Γ_T	Γ_F	Γ_T	Γ_F	Γ_T	Γ_F	Γ_T
Pos fork	17.8	3.4	0.2	4.0	0.3	0.5	0.3	0.0
Ang fork	17.6	31.6	16.7	26.9	1.3	0.7	1.3	0.2
Pos cross	17.0	0.9	0.6	8.0	0.0	0.7	0.3	0.2
Ang cross	5.0	22.0	16.4	25.7	0.2	0.8	0.5	0.2

Table 5 Maximum relative cross bushing force and torque errors [%] for a misalignment angle of $\alpha = 15°$

Cross / *Test*	*Bushing 1*		*Bushing 2*		*Bushing 3*		*Bushing 4*	
	Γ_F	Γ_T	Γ_F	Γ_T	Γ_F	Γ_T	Γ_F	Γ_T
Pos fork	18.7	2.7	0.1	4.8	0.3	0.0	0.2	0.1
Ang fork	7.7	24.9	12.9	20.8	0.5	0.0	0.4	0.1
Pos cross	16.2	2.6	0.3	5.6	0.1	0.1	0.2	0.1
Ang cross	4.9	23.3	17.0	24.1	0.4	0.1	0.4	0.0

Figures 17–20 report the forces and torques acting on the output fork bushings in case of a misalignment angle of $\alpha = 0°$ ($\alpha = 15°$).

Since the influence of the errors introduced is entirely observed on the cross and on the output fork, the forces and torques acting on the bushings of the input fork are not herein reported.

Tables 6 and 7 report the maximum values of the relative fork bushing force and torque plots, considering a misalignment angle of $\alpha = 0°$ and $\alpha = 15°$, respectively. Both the localisation and the angular errors are applied to the output fork bushing 2. The influence on the input fork can be neglected.

Figure 17 Fork bushing force vs input shaft angle θ for misalignment angle of $\alpha = 0°$: (a) Fork bushing 1 and (b) Fork bushing 2

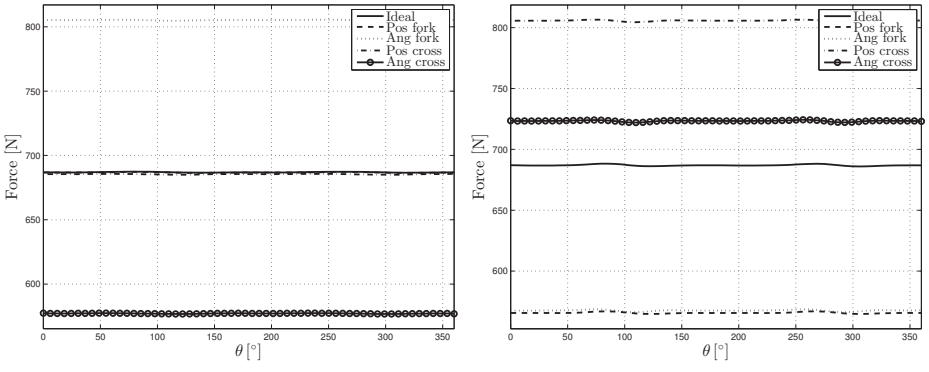

Figure 18 Fork bushing torque vs input shaft angle θ for misalignment angle of $\alpha = 0°$: (a) Fork bushing 1 and (b) Fork bushing 2

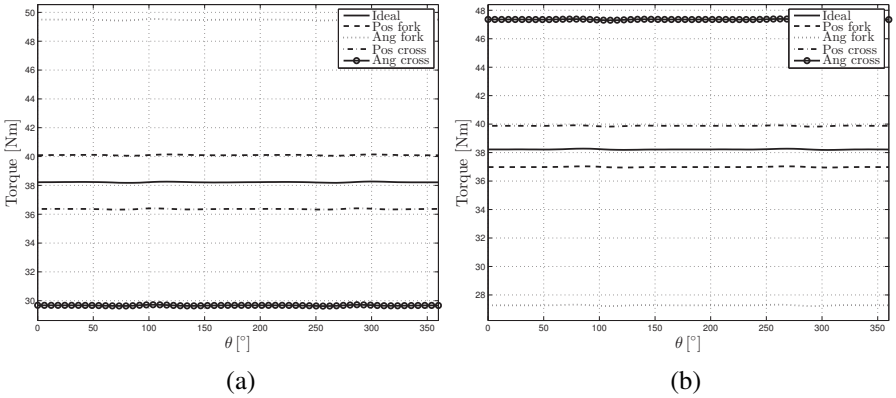

The simulation results for these bushings match the overall dynamic response of the cross bushings. Although the manufacturing errors are applied to specific bushings, their effect influences the dynamic behaviour of most of the joint components. However, the frequency of each reaction force is the same as the ideal case.

Also for the fork bushings the force and torque reactions are mitigated by increasing the angle α from $0°$ to $15°$.

Figures 21 and 22 report the torque generated by the non-linear springs for a misalignment angle of $\alpha = 15°$. Again the dimensional errors introduced in the test cases do not affect the behaviour of the non-linear springs between the cross and the input fork.

Figure 19 Fork bushing force vs input shaft angle θ for misalignment angle of $\alpha = 15^\circ$: (a) Fork bushing 1 and (b) Fork bushing 2

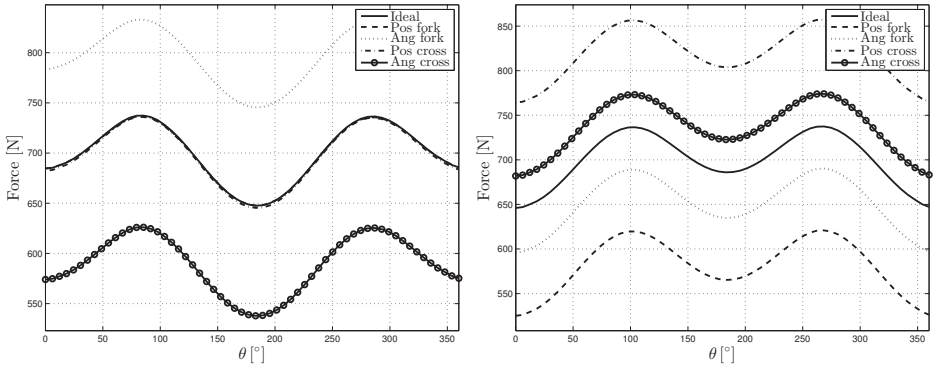

(a) (b)

Figure 20 Fork bushing torque vs input shaft angle θ for misalignment angle of $\alpha = 15^\circ$: (a) Fork bushing 1 and (b) Fork bushing 2

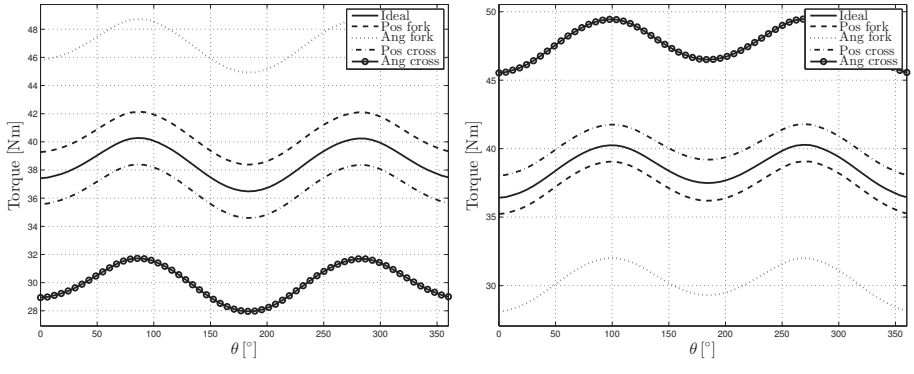

(a) (b)

Table 6 Maximum relative fork bushing force and torque errors [%] for a misalignment angle of $\alpha = 0^\circ$

Test \ *Fork*	*Input fork*				*Output fork*			
	Bushing 1		*Bushing 2*		*Bushing 3*		*Bushing 4*	
	Γ_F	Γ_T	Γ_F	Γ_T	Γ_F	Γ_T	Γ_F	Γ_T
Pos fork	0.2	0.0	0.5	0.2	0.0	4.9	17.7	3.3
Ang fork	1.0	0.1	1.6	0.4	17.1	29.3	17.6	28.8
Pos cross	0.3	0.0	0.0	0.1	0.3	5.0	17.1	4.2
Ang cross	0.5	0.0	0.3	0.1	16.0	22.5	5.1	23.7

Table 7 Maximum relative fork bushing force and torque errors [%] for a misalignment angle of $\alpha = 15^\circ$

Test \ *Fork*	*Input fork*				*Output fork*			
	Bushing 1		*Bushing 2*		*Bushing 3*		*Bushing 4*	
	Γ_F	Γ_T	Γ_F	Γ_T	Γ_F	Γ_T	Γ_F	Γ_T
Pos fork	0.1	0.9	0.4	0.8	0.1	4.6	18.7	3.5
Ang fork	0.3	1.1	0.6	0.9	12.9	20.9	7.7	22.8
Pos cross	0.2	0.8	0.3	0.9	0.3	5.2	16.2	3.7
Ang cross	0.5	0.9	0.3	1.0	17.0	23.4	4.9	22.7

Figure 21 Non-linear springs between the cross and the input fork for a misalignment angle of $\alpha = 15^\circ$: (a) non-linear springs 1-2 and non-linear springs 3-4

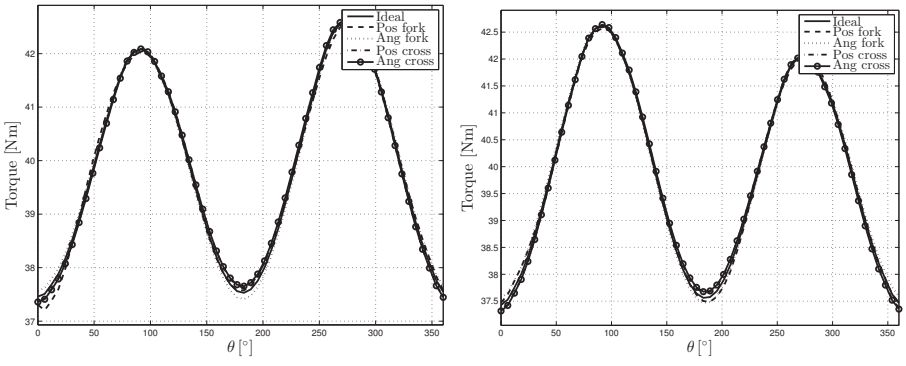

(a) (b)

Figure 22 Non-linear springs between the cross and the output fork for a misalignment angle of $\alpha = 15^\circ$: (a) non-linear springs 5-6 and (b) non-linear springs 7-8

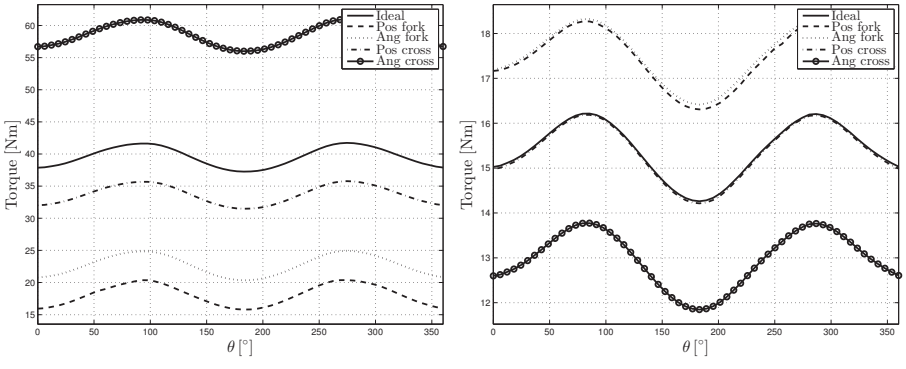

(a) (b)

5 Conclusion

A multibody model of a Cardan joint based on penalty forces and discrete flexible bodies has been presented.

The bushing elements and the non-linear springs have been characterised according to structural and compliance properties. Elastic deformations allow to simulate the effect of manufacturing errors, otherwise difficult with a constraint-based multibody approach.

The numerical simulations proved compatibility with a `GSTIFF` solver. Despite the initial transition phase, the results does not show any numerical instability.

Manufacturing errors applied to the output forks and to the cross produce a coherent distribution of internal reactions on the entire assembly.

Considering a fine tolerance precision, in the worst case, the reaction torques reached 31% higher than the ideal case. The greatest influence on the Cardan joint dynamics is due to the angular errors. However, the new arrangement of forces and torques did not influenced the frequency content.

To allow a wide use of this investigation results, the model has been developed within the framework of CAE software tool.

Ideal geometries of Cardan joints should be avoided when simulating vibrations and fatigue in high-efficient transmission drivelines or during tolerance allocation studies.

The methodology discussed in this paper can also be extended to investigate the influence of different types of manufacturing errors and can be applied to other overconstrained mechanisms.

References

Askari, E., Flores, P., Dabirrahmani, D. and Appleyard, R. (2014) 'Nonlinear vibration and dynamics of ceramic on ceramic artificial hip joints: a spatial multibody modelling', *Nonlinear Dynamics*, Vol. 76, No. 2, pp.1365–1377.

Brutti, C., Coglitore, G. and Valentini, P.P. (2011) 'Modelling of 3d revolute joint with clearance and contact stiffness', *Nonlinear Dynamics*, Vol. 66, 531–548.

Cavacece, M., Pennestrì, E., Valentini, P.P. and Vita, L. (2004) 'Mechanical efficiency analysis of a cardan joint', *ASME Design Engineering Technical Conference*, Salt Lake City, USA.

Cavacece, M., Stefanelli, R., Valentini, P. and Vita, L. (2005) 'A multibody dynamic model of a cardan joint with experimental validation', *ECCOMAS Multibody Dynamics Thematic Conference*, Madrid, Spain.

Cecchini, E., Ettore, P. Stefanelli, R. and Vita, L. (2004) 'A dual number approach to the kinematic analysis of spatial linkages with dimensional and geometric tolerances', *Proceedings of the ASME 2004 International Design Engineering Technical Conferences and Computers and Information in Engineering Conference*, Vol. 2, No. 1, pp.841–849.

Chen, C.K. and Freudenstein, F. (1986) 'Dynamic analysis of a universal joint with manufacturing tolerances', *Journal of Mechanisms, Transmissions and Automation in Design*, Vol. 108, pp.524–532.

Daskalov, A.Y. (1990) 'Kinematic analysis of cardan drives', *Mechanism and Machine Theory*, Vol. 25, No. 5, pp.479–486.

Fischer, I. and Freudenstein, F. (1984) 'Internal force and moment transmission in a cardan joint with manufacturing tolerances', *Journal of Mechanisms, Transmissions and Automation in Design*, Vol. 106, pp.301–311.

Hummel, S.R. and Chassapis, C. (2000) 'Configuration design and optimization of universal joints', *Mechanism and Machine Theory*, Vol. 35, pp.463–476.

Rameau, J-F., Serré, P. and Moinet, M. (2019) 'Clearance vs. tolerance for mobile overconstrained mechanisms', *Mechanism and Machine Theory*, Vol. 136, No. 1, pp.284–306.

Koutsovasilis, P. and Fruth, T. (2012) 'Cylindrical clearance linkages in multibody dynamics - contact analysis and automatisation', *2nd Joint International Conference on Multibody System Dynamics*, Stuttgart, Germany.

Krishna, V., Naganathan, N.G., Phadnis, R. and Dukkipati, R.V. (2000) 'Analysis of driveline loads in an automotive powertrain with multiple cardan joints', *International Journal. Series C, Mechanical Systems, Machine Elements and Manufacturing*, Vol. 214, No. 5, pp.509–522.

Park, T., Haug, E.J. and Yim, H.J. (1988) 'Automated kinematic feasibility evaluation and analysis of mechanical systems', *Mechanism and Machine Theory*, Vol. 23, No. 5, pp.383–391.

Pezzuti, E., Stefanelli, R., Valentini, P.P. and Vita, L. (2006) 'Computer aided simulation and testing of spatial linkages with joint mechanical errors', *International Journal for Numerical Methods in Engineering*, Vol. 35, pp.1735–1748.

Seherr-Thoss, H.C., Schemelz, F. and Aucktor, E. (2006) *Universal Joints and Driveshafts*, 2nd ed., Springer, Berlin, Germany.

Sheu, P.P., Chieng, W.H. and Lee, A.C. (1996) 'Modeling and analysis of the intermediate shaft between two universal joints', *Journal of Vibration and Acoustics*, Vol. 118, No. 1, pp.88–99.

Valentini, P.P. (2014) 'Effects of dimensional and geometrical tolerances on kinematic and dynamic performances of rzeppa ball joint', *Institution of Mechanical Engineers, Part D: Journal of Automobile Engineering* Vol. 228, pp.37–49.

Valentini, P.P. and Pezzuti, E. (2011) 'Effects of geometrical and dimensional errors on kinematics and dynamics of tracta coupling', *Journal of Theoretical and Applied Mechanics*, Vol. 49, No. 1, pp.117–133.

Wojtyra, M. (2009) 'Joint reactions in rigid body mechanisms with dependent constraints', *Mechanism and Machine Theory*, Vol. 44, No. 2, pp.2265–2278.

Young, W., Budynas, R. and Sadegh, A. (2011) *Roark's Formulas for Stress and Strain*, McGraw Hill Professional.